Research Square

Preprints are preliminary reports that have not undergone peer review.
They should not be considered conclusive, used to inform clinical practice,
or referenced by the media as validated information.

Optimized 3d printability and stability of low-methylated pectin-xyloglucan-cellulose nanocrystal composites

Smarak Bandyopadhyay
Institute of Agrophysics, Polish Academy of Sciences
Vadym Chibrikov
Institute of Agrophysics, Polish Academy of Sciences
Katarzyna Grygorczuk-Płaneta
Institute of Agrophysics, Polish Academy of Sciences
Karolina Fila
Institute of Agrophysics, Polish Academy of Sciences
Abitha Puzhakkara Veettil
Institute of Agrophysics, Polish Academy of Sciences
Justyna Cybulska
Institute of Agrophysics, Polish Academy of Sciences
Katarzyna Szewczuk-Karpisz
Institute of Agrophysics, Polish Academy of Sciences
Artur Zdunek
a.zdunek@ipan.lublin.pl

Institute of Agrophysics, Polish Academy of Sciences

Article

Keywords: Pectin, hemicellulose, cellulose, 3D printing, rheology

Posted Date: July 28th, 2026

DOI: https://doi.org/10.21203/rs.3.rs-10341614/v1

License: This work is licensed under a Creative Commons Attribution 4.0 International License.
Read Full License

Additional Declarations: No competing interests reported.

Optimized 3d printability and stability of low-methylated pectin-xyloglucan-cellulose nanocrystal composites

Smarak Bandyopadhyay[†] [a], Vadym Chibrikov[†] [a], Katarzyna Grygorczuk-Płaneta [a], Karolina Fila [a], Abitha Puzhakkara Veettil [a], Justyna Cybulska [a], Katarzyna Szewczuk-Karpisz [a], Artur Zdunek * [a]

[a] *Institute of Agrophysics, Polish Academy of Sciences, ul. Doświadczalna 4, Lublin 20-290, Poland*

† *These authors contributed equally to this work*

*corresponding author: Artur Zdunek, Institute of Agrophysics, Polish Academy of Sciences, Doświadczalna 4 Str., 20–290 Lublin, Poland, e-mail: a.zdunek@ipan.lublin.pl; phone: +48 817 445 061; fax: +48 817 445 067

ABSTRACT

Extrusion-based 3D printing of biobased hydrogels depends on ink rheology, requiring strong shear-thinning for smooth flow and sufficient yield stress to maintain shape after deposition. Polysaccharides from plant cell walls (PCW) are known as sustainable, structurally stable materials, but their three main components—cellulose, hemicellulose, and pectin—have not been combined for this purpose. Here, a bioink composed of cellulose nanocrystals, xyloglucan, and pectin is developed for extrusion printing using response surface methodology (RSM) with material characterization. Systematic variation in composition reveals clear relationships between rheology, print fidelity, and mechanical performance. FTIR confirms composition-dependent hydrogen bonding within inks and printed structures, along with formulation-dependent colour changes. Among the components, pectin has the strongest influence on rheology. Biobased inks with equal proportions of all three components (3% and 5%) show optimal printability. Compared to 3%, 5% formulations exhibit higher viscosity and yield stress, improving shape retention and pore definition. Ionic cross-linking does not significantly affect geometry but enhances mechanical strength. These findings highlight multicomponent plant polysaccharide inks as tunable, sustainable materials for extrusion-based additive manufacturing, mimicking natural PCW assembly.

KEYWORDS Pectin, hemicellulose, cellulose, 3D printing, rheology

1. INTRODUCTION

Three-dimensional (3D) printing is an advanced manufacturing technology that offers exceptional opportunities for customization, design flexibility, and sustainability through the layer-by-layer deposition of materials to create tailored geometries [1,2]. Among the various 3D - printing techniques, extrusion-based printing has gained increasing attention, with its success largely governed by the rheological properties of the printing ink [3].

Collapse of the printed structure and its shape fidelity are common challenges in the case of biobased hydrogels used for 3D printing. Suitable materials for 3D printing should exhibit rheological properties that enable them to flow readily through the nozzle while the gel forms. It means that the ink should show the shear-thinning visco-elastic properties, so viscoelastic materials can extrude smoothly through the nozzle. However, the exhibition of self-supporting properties after extrusion requires a viscoelastic response of the material with a finite yield stress to resist post-print collapse [4]. Understanding the rheological behavior of the materials is therefore necessary to design inks, nozzles and extrusion conditions to print 3D printed composites with optimal resolution and fidelity. Although a wide range of feedstock has been explored, recent efforts have focused on replacing conventional materials with more sustainable and environmentally friendly alternatives, including plant cell wall polysaccharides.

Among plant-derived polysaccharides, nanocellulose has been most extensively investigated for direct ink writing due to its biocompatibility, biodegradability, and excellent mechanical performance [1,2]. Pectin has emerged more recently as a promising material for direct ink writing [5–7], while unmodified hemicelluloses extracted from various biomass sources have also been incorporated into printable formulations [8,9]. Despite these advances, most current studies focus on simplified systems comprising one or two components, thereby failing to fully leverage the inherent structural complexity and interactions among the respective plant cell wall polysaccharides. Moreover, the extensive natural diversity and tunability of plant cell wall polysaccharides in the context of 3D printing remain largely unexplored.

Therefore, inspired by the natural assembly of plant cell wall, we hypothesize in this research that combinations of three polysaccharides (pectin, xyloglucan and cellulose) will allow formulation of extrusion-based 3D-printing inks with tunable rheological properties. By systematically varying polysaccharide composition, this work seeks to establish correlations between ink rheology and the resulting mechanical and structural properties of the printed

constructs, offering a sustainable and conceptually transferable framework for advanced bio-based materials in additive manufacturing. Demonstration of satisfactory printability from the inks made of three major polysaccharides assembling the plant cell wall and possible tunability of prosperities of printed biomaterials are the main novelties of this research.

2. MATERIALS & METHODS

2.1. Characterizations of carbohydrates:

The low methylated pectin (LMP) was procured from Herbstreith & Fox GmbH (Neuenbürg, Germany). Tamarind seed xyloglucan (XG) was supplied by Megazyme (Bray, Ireland) and Neogen iEMEA (Ayr, UK). Calcium chloride ($CaCl_2$) was provided by Sigma-Aldrich (Darmstadt, Germany). Cellulose nanocrystals (CNC) were delivered by Nanografi (Ankara, Turkey).

Detailed methodology for chemical analysis is mention in Supplementary Section M1. Chemical composition and structure of respective PCW polysaccharides is provided in Supplementary Table S1.

2.2. Experimental design and preparation of ink formulations:

A central composite design was used to make 15 compositions utilizing different concentrations of LMP, CNC and XG (Supplementary Table S2). The factorial points (+1 and -1 levels) for each factor were 1.2 and 5.0 (based on preliminary results not reported here), axial points (+α and -α levels) 0.0 and 6.3, center point (0) 3.1 respectively. Each composition was made in a 100 mL volume with deionized water and homogenized in a 150 mL glass beaker at 30,000 rpm for 30 min with S 10 N - 8 G ST Dispersing tool in IKA T 10 Basic Ultra-Turrax® Homogeniser (IKA-Werke GmbH & Co. KG, Germany). The inks were stored at ci. 4 °C prior further analysis.

2.3. Physiochemical properties of ink formulations:

For the designed ink formulations, color evaluation was done using Lovibond TR 500 (The Tintometer Ltd, UK) with 8 mm aperture. The apparatus was calibrated against a standard black and white provided with the instrument. The color of the ink was measured in glass beaker and the glass beaker with standard water was used as a reference. The Delta E (ΔE) was calculated using the **Equation (1)**:

$$\Delta E = \sqrt{(\Delta L^*)^2 + (\Delta a^*)^2 + (\Delta b^*)^2}, \text{ where:} \quad \textbf{(1)}$$

where, *(L) lightness, (a) red/green, and (b) yellow/blue are the elements of the color*

The white index (WI) was calculated as per the method reported by da Silva Bruni et al. [10]

2.4. Rheological properties of ink formulations:

Discovery Series Hybrid Rheometer HR-1 (TA Instruments, USA) with a 20 mm parallel plate geometry was used to measure the rheological properties. All the samples were conditioned before analyzing at 25 °C for 240.0 s. Viscosity was analyzed by flow-peak hold at low shear rate ($1s^{-1}$) and high shear rate ($100s^{-1}$) for 80.0 s at 25 °C.

The shear rate ramp analysis was done from 0.1 to 100 s^{-1} following a flow sweep method with steady state sensing and 25 points per decade. The shear stress – shear rate results were fitted with the Casson model [11] as calculated by the **Equation (2)**:

$$\tau = \sqrt[n]{\tau_0 + (\dot{\gamma} * \eta_p)^n}, \quad \textbf{(2)}$$

τ represents the shear stress, $\dot{\gamma}$ is the shear rate, τ_0 is represented as the yield stress, η_p is plastic viscosity.

The thixotropic behavior was observed by continuing the shear rate ramp from 100 to 0.1 s^{-1}.

2.5. Molecular properties of ink formulations:

The Fourier Transform Infrared spectroscopy (FTIR) characterization of the inks and printed structures was performed using a Nicolet iS50 (Thermo Scientific, USA) with an attenuated total reflectance accessory (Smart iTX_Diamond ATR), DTGS-KBr detector and the Omnic Software (Version: 2.20). The defined spectral range for samples and background (air) was from 4000–400 cm^{-1} with a resolution of 4 cm^{-1} and 64 scans per analysis.

2.6. 3D-printing of biomaterial structures

For composite 3D printing, the direct ink writing technique was used. Batch printing was performed with BIO X 3D bioprinter (CELLINK, Sweden) using 3mL pneumatic printhead. Ready-to-use ink formulations were transferred to the 3 mL printing syringe immediately after preparation or post ink preparation processing, when stored for later usage.

Depending on the rheological properties of ink formulations, the printing pressure was adjusted in a range of 20-200 kPa. All composites were printed with 22G (0.41 mm internal diameter) conical bioprinting nozzles (CELLINK, Sweden/Adhesive Dispensing Ltd, UK), with a constant printing speed of 5 mm/s. Printability of ink formulations was assessed by printing three principal objects – single lines, grid, and a cylinder. Object models were created in *DNA Studio 4.1.3* (CELLINK, Sweden). Model file for a single line prints had the encoded line length of 20 mm, width of 0.41 mm, with a three consecutive lines printed on a laboratory glass. The model for the grid had an input description of 30 × 30 × 3 mm with 10% infill density and 7-layer structure. The cylinder structure had a defined height and diameter of 10 mm, printed with a 50% infill density and as a 24-layer structure.

To access a temperature-driven gelation of XG [12], as well as ion-based gelation ageing of LMP [13], 3D printed composites were completely soaked in 14.32 mM $CaCl_2$ (Sigma-Aldrich, Germany) aqueous solution for 30 min, followed by 4 ℃ exposure overnight. Current samples were referred to as *treated,* while those with no treatment were defined as *natural*.

2.7. Evaluation of biomaterial ink printability and shape retention properties:

To access data on ink formulation printability and shape retention properties of 3D printed biomaterial structures, a set of principal parameters was calculated for both single-line prints and grid prints.

For single-line prints, the uniformity factor (descriptor of the homogeneity of a longitudinal line profile), line length, and line width were calculated according to Merli et al. [14] with a revised methodological approach. For that purpose, home-made scripts were prepared, which allowed for both automated/manual object detection, midpoint line definition, as well as length evaluations of both local perpendiculars and the midpoint line [15]. Uniformity factor was evaluated according to **Equation (3)**:

$$U = 1 - \frac{\Delta D}{D_{mean}}, \text{ where:} \quad \textbf{(3)}$$

U – the uniformity factor (a.u.); 1 – homogeneous longitudinal line profile; <1 – edge imperfections along longitudinal line profile;

ΔD – the standard deviation of a fiber diameter (metric/pixel units);

D_{mean} – the mean fiber diameter (metric/pixel units).

For a line length evaluation, the midpoint line was chosen, while for line width, a set of local perpendiculars was determined with a gap of 50 µm approximately. For the transition to metric units, a scaling factor was calculated by capturing the calibration scale.

As for the grid prints, shape retention properties were assessed by evaluating the total grid area, grid area (excluding pores), perimeter coefficient, and grid extent (grid length and width) (Chibrikov, 2025). Total grid area, as a descriptor of an area occupied by both the grid and its pores, was calculated according to **Equation (4)**:

$$A_t = A_g + A_p, \text{ where:} \quad \textbf{(4)}$$

A_t – the total grid area (mm^2);

A_g – the grid area (mm^2);

A_p – the total pore area (mm^2).

The perimeter coefficient was calculated according to Merli et al. [14] with a revised methodological approach. Here, home-made scripts were also prepared allowing for both manual/automatic pore detection, centroid and perpendiculars evaluation, and its length calculation [15]. Perimeter coefficient, which is a descriptor of the homogeneity of a longitudinal and transverse edge profiles, was calculated according to **Equation (5)**:

$$P_e = \frac{1}{\left\{\left[0.5\times\left(\frac{L_x^{exp}}{L_x}+\frac{L_y^{exp}}{L_y}\right)-1\right]+1\right\}\times\left[1+0.5\times\left(\frac{\Delta L_x^{exp}}{L_x}+\frac{\Delta L_y^{exp}}{L_y}\right)\right]}, \text{ where:} \quad \textbf{(5)}$$

P_e – the perimeter coefficient (a.u.); 1 – square grid; <1 – grid shape distorted.

L_x^{exp} – the mean length (x axis) of the printed geometry (pixel/metric units);

L_y^{exp} – the mean width (y axis) of the printed geometry (pixel/metric units);

ΔL_x^{exp} – the standard deviation of a length (x axis) of the printed geometry (pixel/metric units);

ΔL_y^{exp} – the standard deviation of a width (y axis) of the printed geometry (pixel/metric units);

L_x – the theoretical length (x axis) of the printing geometry (pixel/metric units);

L_y – the theoretical width (y axis) of the printing geometry (pixel/metric units).

For the transition to metric units, a scaling factor was calculated by capturing the calibration scale.

Also, data on pore shape retention properties were assessed by evaluating pore area, pore area retention, pore factor, and pore perimeter. Pore area retention was calculated as an actual ratio of the area occupied by grid pores to its model value. To evaluate pore factor as a descriptor of pore shape deviation, homemade scripts were prepared (Chibrikov, 2025). Pore factor was evaluated according to **Equation (6)**:

$$P_r = \frac{P^2}{16A}, \text{ where:} \quad \textbf{(6)}$$

P_r – the pore factor (a.u.); 1 – perfectly square pore; <1 – circular pore; >1 – elliptical pore.

P – the pore perimeter (metric/pixel units);

A – the pore area (metric/pixel units).

For the transition to metric units, a scaling factor was calculated by capturing the calibration scale. All of the aforementioned structures were captured with a GR III (Ricoh Imaging Company Ltd., Japan) digital camera, equipped with a 28 mm lens, at a resolution of appr. 15-25 μm/pixel.

2.8. Morphological characterization of 3D biomaterial structures:

The morphology of 3D printing grid composites incorporating polysaccharides was observed using a scanning electron microscope (SEM, Phenom ProX, Thermo Scientific, USA). Before analysis, the 3D printed grids were soaked in 14.32 mM $CaCl_2$ for 30 minutes followed by 4 °C exposure overnight and later placed in a freeze dryer for 7 days. Cross-sectional images were acquired at 500× magnification at an accelerating voltage of 15 kV with a BSD detector. The pores size was analyzed using ImageJ representing average of 10 measurements.

2.9. Mechanical properties of 3D-printed biomaterial structures:

Macroscale mechanical properties of 3D-printed biomaterial structures were assessed by means of a compression test. The specimen's testes comprised a cylinder with a diameter of 10 mm, a height of 10 mm, printed with an infill volume of 50%. The uniaxial tensile tests at a constant strain rate were performed using a Lloyd LRX material testing machine (Ametek, Denmark) equipped with a 10 N load cell, and an 11 mm flat indenter. The specimens were subjected to a uniaxial tensile test with a constant compression rate of 20 mm/min until 10% of compression to exclude the substrate effects. The Young's modulus (elastic deformation curve slope), maximum stress, toughness (energy required to fracture a sample) and work of deformation (total energy absorbed) were extracted using a homemade Python script [15].

2.10. Data processing and statistical design:

Experimental design and data analysis were performed using *Design-Expert*® software (Stat-Ease, Inc., USA). Data analysis and visualization were performed in *RStudio 2025.09.1 Build 401* (Posit Software, USA). Differences were analyzed using three-way (ink composition, printing pressure, and cross-linking treatment; if other was not mentioned) analysis of variance (ANOVA) and the Tukey test for honestly significant differences at the significance level $p = 0.05$.

3. RESULTS & DISCUSSIONS

3.1. Optimization and statistical evaluation of printing ink rheology

The rheological optimization was performed using a response surface design incorporating three formulation factors—LMP, XG, and CNC—each assessed at three levels, with three responses: viscosity (μ) at shear rates of 1 and 100 s^{-1}, and yield stress (σ_γ). The full design structure is provided in Supplementary Table S2. Inclusion of axial points in the central composite design (CCD) enabled accurate estimation of the coefficients of a second-order polynomial model (**Equation 7**), from which the factorial effects were determined [16]

$$Y = \beta_0 + \beta_1 X_1 + \beta_2 X_2 + \beta_3 X_3 + \beta_{11} X_1^2 + \beta_{22} X_2^2 + \beta_{33} X_3^2 + \beta_{12} X_1 X_2 + \beta_{13} X_1 X_3 + \beta_{23} X_2 X_3 + \epsilon \quad \textbf{(7)}$$

X_1, X_2 and X_3: Factors LMP, XG and CNC, respectively

Y: The response (dependent variable)

β_0: The intercept (constant)

β_1, β_2 and β_3: Linear coefficients for factors X_1, X_2 and X_3

β_{11}, β_{22} and β_{33}: Quadratic (curvature) coefficients for X_1^2, X_2^2 and X_3^2

β_{12}, β_{13} and β_{23}: Interaction coefficients for $X_1 X_2$, $X_1 X_3$, and $X_2 X_3$

ϵ: The random error term

As summarized in Supplementary Table S3, the Model F-values of 226.09, 138.4 and 173.98 demonstrate that all the models are highly significant, with only a 0.01% likelihood that such large F-values arise from noise. Model terms with p-values below 0.05 were considered statistically significant. In all three quadratic models, terms A, B, C, and interactions met this requirement, whereas two interaction terms with p-values above 0.10 were deemed non-significant. The Predicted R^2 values showed good agreement with the Adjusted R^2 (difference < 0.2; Supplementary Table S4), confirming internal consistency. Adeq Precision values of 48.95, 37.94 and 43.37 exceeded the threshold of 4, demonstrating an adequate signal-to-noise ratio. Collectively, these metrics indicate that the model is appropriate for navigating the experimental design space.

The normal probability plots used to evaluate the models (Fig. 1a–c) show the plots for standardized residuals of viscosity at low shear rate (μ *at* $1s^{-1}$ γ), high shear rate (μ *at* $100s^{-1}$ γ) and yield stress (σ_γ). In such plots, points aligning closely with a straight line, like those in Fig. 1, indicate that residuals follow a normal distribution. Minor deviations are typical even for normally distributed data. Thus, the residuals for some models' responses can reasonably be viewed as normally distributed [17]. Also the residuals-verses-predicted plot and residuals-verses-run plot (Supplementary Fig. F1 and F2) pass the diagnostic tests by showing points scattered

randomly (Supplementary Fig. F1) and exhibiting no trends, shifts or outliners (Supplementary Fig. F2), respectively. The Box-Cox plot (Supplementary Fig. F3) also shows that the responses for all three models falls within the red-lined confidence interval. All these statistical validities together helped to judge and accept the model.

In an orthogonal design, the intercept represents the overall average response across all experimental runs. In the present study, Supplementary Table S5 clearly illustrates this, with the intercept serving as the baseline from which factor effects are interpreted. Each coefficient reflects the deviation from this average when a given factor changes by one unit while the remaining factors are held constant.

Although viscosity and yield stress increase progressively with increasing concentrations of LMP, XG, and CNC (Fig. 2), the magnitude of these contributions differs among components (Supplementary Table S5). All three factors significantly influence the rheological responses; however, LMP exerts the greatest effect, followed by XG, with CNC exerting the smallest impact.

The Design-Expert software evaluated the full factor ranges and generated multiple candidate solutions for maximizing the responses. Of the 62 possible solutions, the one recommended by the software is presented in Supplementary Table S6. CCD is particularly advantageous for developing accurate predictions near the centre of the design space. Centre points, incorporated into the CCD, provide an estimate of pure error and support the lack-of-fit test, thereby strengthening the statistical reliability of the fitted quadratic model. Their inclusion enhances the robustness and precision of the response surface, especially when identifying optimal conditions [18].

Compared with other screening designs such as the Plackett–Burman design, CCD requires fewer experimental runs while demanding less computational expertise, making it an efficient approach for formulation optimization. A key challenge, however, lies in identifying the critical factors that most strongly govern the responses. CCD is also well suited for sequential experimentation because it can extend earlier factorial designs by adding axial and centre points [18].

To highlight the role of CCD centre points in the present study, an intermediate concentration (3.18% w/v) was included alongside the highest response-generating factorial point (5.07% w/v), for further investigations, thereby allowing more reliable curvature estimation and confirming the validity of the optimized formulation.

An optimal 3D-printing ink must exhibit pronounced shear-thinning behavior to ensure smooth extrusion and stable filament formation, along with sufficient thixotropy to enable rapid viscosity recovery after deposition [19]. A similar rheological profile was observed for both

composite-based inks evaluated in the present study, each demonstrating the shear-dependent flow and structural recovery characteristics required for reliable printing performance (Fig. 3).

3.2. Physicochemical properties of ink formulations

Color parameters, as well as the whiteness index of 3% (LMP-XG-CNC) and 5% (LMP-XG-CNC) 3D printing ink formulations is provided in Supplementary Table S7. Trend in lightness and whiteness index increase with an increasing CNC content facilitate closer (smaller that the wavelength of visible light) particle packing in ink formulations, enhancing it structural organization [20]. This organized network intensifies multiple light scattering events within the ink formulation matrix while minimizing its absorption. Both a^* and b^* axis shifts support the notion. As the light bounces more times within the denser 5% (LMP-XG-CNC) ink formulations prior escaping, shorter wavelengths (blue/green) are scattered more effectively. It leaves the longer wavelengths (yellow/red) to dominate the perceived color of an ink formulations, and, as evidenced later on, of a 3D printed composites.

Furthermore, the total color difference between the ink formulations allows to suggest that CNC content is a primary driver of the optical profile, likely due to the development of a denser CNC-based scaffold that effectively reflects the visible light spectrum [21]. In turn, there are evidences that may show the contribution of LMP [22] and XG [23] in such an ink formulations.

3.3. Molecular properties of ink formulations and 3D-printed biomaterial structures

The commercial PCW (LMP, XG and CNC) contains fractions of rhamnose, fructose, arabinose, xylose, mannose, galactose, glucose, and uronic acid as specified in Supplementary Table S1. LMP was composed primarily of homogalacturonan (90.98 mol%), calculated as the difference between uronic acids and rhamnose content [24], which contained 44.64 ± 2.12 methylated carboxyl groups. The main components of XG were glucose (51.69 ± 0.24), xylose (29.58 ± 0.08) and galactose (15.94 ± 0.01), while CNC consisted of glucose (95.90 ± 0.03) with a negligible content of other monosaccharides characteristic of cell walls.

Macromolecular characterization using the SEC-MALLS method was conducted for LMP and XG, as CNC did not dissolve in water-based mobile phase (Supplementary Table S1). XG was characterised by a significantly higher molecular weight (Mn and Mw) and low polydispersity (PDI~1.06) compared to LMP, indicating a more homogeneous population of molecules. Despite its higher molecular weight, XG exhibited lower values of radius of gyration, viscometric hydrodynamic radius and intrinsic viscosity, indicating a smaller hydrodynamic volume of its molecules in solution. LMP was characterised by significantly higher intrinsic viscosity, larger radius of gyration and hydrodynamic radius, and approximately twice the polydispersity, indicating greater heterogeneity of molecular fractions and stronger hydration

of pectin chains. Analysis of the conformational plot slope (log Rg versus log Mw) revealed significant differences in the spatial organisation of the studied polysaccharides: the slope for LMP (0.28±0.03) suggested a sphere-like conformation in the hydrated state, while the higher slope value for XG (0.58±0.04) was characteristic of a random coil conformation. These results indicate that despite the smaller hydrodynamic size of XG molecules, their global spatial organisation differs significantly from the more globular structure of LMP.

The IR spectra (Fig. 4) highlight distinct spectral regions characteristic of polysaccharides [25]. The FTIR spectra of the raw materials are shown in Supplementary Fig. F4 and F5. The variations in the OH stretching intensity, at 1635 cm^{-1}, among the different 3D-printed structures (Fig. 4a) likely reflect differences in hydrogen-bonding interactions [26]. As noted by Pękala et al. [27], xyloglucan (XG) binds more strongly to cellulose than pectins, whereas pectins can still associate with cellulose when hemicellulose levels are low. Given that hydrogen bonding is a major contributor to interactions within PCW, similar behavior is evident in our results (Fig. 4a).

Across region I (4000–2500 cm^{-1}; Fig 4a), the OH stretching band shows highest intensity for XG-CNC, followed by LMP-CNC and LMP-XG. The OH band intensity also increases when polysaccharide content increases from 3 to 5% (Fig. 4b), likely due to enhanced hydrogen bonding or greater bound water. Region II (Fig. 4a) contains peaks consistent with commercial apple pectin and microcrystalline cellulose, in agreement with Liu et al. [28].

In region IV, the polysaccharide fingerprint region, peaks 1–7 demonstrate compositional effects on band intensities (Fig. 4a). Peak 1 at 1159 cm^{-1} reflects C-O-C glycosidic linkages [29] between xylose [30], a key structural element of XG. The increased intensity of this band at higher XG levels aligns with HPLC data (Supplementary Table S1). The 1143 cm^{-1} peak is more pronounced in formulations richer in rhamnose, a major RG-I component [31], in the tested materials, a weekly marked peak may indicate the presence of ramnogalacturonan, or be the result of C-O vibrations in the pyranose ring. Peak 2 (1072–1110 cm^{-1}) corresponds to the C-O stretching [32]. Peak 3 at 1052 cm^{-1} is attributed to cellulose [28] and is absent in LMP-XG, where CNC is not included.

The FTIR spectra of the PCW polysaccharides, as well as solutions, used in current study are shown in Supplementary Fig. F4 and F5.
Peak 4 shows vibrational bands at 1029 cm^{-1} (XG-CNC) and 1010 cm^{-1}, characteristic of cellulose and pectins/XG, respectively [28,33,34]. Peak 5 at 949 cm^{-1} (Fig. 4a, Supplementary Table S1) likely reflects mannose content in the polysaccharide blends [28]. Peaks 6 (890 and 893 cm^{-1}) correspond to XG from tamarind seed, arabinose, and crystalline cellulose [28]. Peak 7 at 831 cm^{-1} is associated with apple pectin [28], explaining its absence in XG-CNC.

Comparisons, presented in Fig. 4b, between the ink composed of all three polysaccharides (LMP-XG-CNC) and lyophilized 3D printed structures reveal notable differences. In region I(a), the OH stretching varies substantially due to differences in water content (Fig. 4b). In region II, the ~1635 cm^{-1} band intensity also differs between ink and 3D structures, reflecting varying water interactions [25]. The ~1620 cm^{-1} peak corresponds to ionic free carboxylate groups ($–COO^–$), while the ~1730 cm^{-1} band represents esterified carboxyl groups ($–COOCH_3$) [26,35].

In region IV (Fig. 4b), peak 1 splits into two signals: 1148 cm^{-1} in 3D structures and 1128 cm^{-1} in inks, both proportional to polysaccharide content. The 1148 cm^{-1} band corresponds to pectins [32], while the 1128 cm^{-1} peak aligns with arabinose present (Supplementary Table S1) in all raw materials [28]. Peaks 2 and 3 follow the same assignments as in Fig. 4a, though they display reduced intensity and sharper features in inks, likely due to changes in hydrogen bonding. Peaks 4, 5, 6, and 7 (1010, 949, 893, and 831 cm^{-1}) are not present in the ink formulations and appear only in the 3D structures (Fig. 4b).

3.4. Printability and shape-retention properties of 3D printed biomaterial structures

As a primary structural element of a print, line shape directly governs the pore architecture and mechanical performance of the final scaffold. As for the natural samples, printed lines tended to collapse and merge, suggesting a lack of meaningful insights into shape retention properties. Therefore, data on line shape retention properties of treated samples only were evaluated and are represented in Fig. 5. Characterized by lower viscosity, the 3% (LMP-XG-CNC) samples showed a smoother edge surface, as evidenced by a narrower data distribution of the uniformity factor (Fig. 5a). For the 5% (LMP-XG-CNC) samples, the uniformity factor data distribution was more prominent. It was evidenced by analyzing line width as a function of line length (Supplementary Fig. F6), suggesting that the higher concentration of solids results in a rougher line edge. Indeed, increasing cellulose concentration has been previously reported not only to ensure the structural fidelity of 3D printed structures but also to introduce surface irregularities due to higher ink yield stress and increased nozzle friction [36]. Driven by higher solid matter content, such edge roughness may significantly limit the visual appearance of the final product (smoothness, texture), as well as its structural (interlayer adhesion), physicochemical (permeability, swelling ability), and mechanical (crack formation) properties [37].
Conversely, the line width of the 5% (LMP-XG-CNC) samples was closer to the initial model, showing a statistically significant increase with rising printing pressure (Fig. 5b). The same trend was observed for the 3% (LMP-XG-CNC) samples, yet the actual values were almost twice those defined by the model. Here, the inferior line shape retention of the 3% (LMP-XG-CNC) samples compared to the 5% (LMP-XG-CNC) samples is attributed to high water content and lower viscosity, leading to significant post-extrusion spreading [38].

Regarding line length, the values remained consistent with the models, though they were statistically significantly lower for the 5% (LMP-XG-CNC) samples (Fig. 5c). To account for the diverse rheological behaviors of biomaterials, manufacturers often include pre-printing and post-printing delay parameters in bioprinting software (Supplementary Fig. F7) [39]. These adjustments allow for the synchronization of ink extrusion with nozzle movement, thereby compensating for the non-Newtonian, shear-thinning behavior of the ink.

Data on the shape retention properties of the 3D printed biomaterial grids are shown in Fig. 6. The data confirm that the studied LMP-XG-CNC inks can be used for precision printing, mainly resembling model structures. The values for the total grid area, as a descriptor of the area occupied by both the grid and its pores, were close to those predefined by the model (Fig. 6a). On average, the total grid area of the treated samples was statistically significantly higher, compared to the natural samples, which is attributed to water swelling. In turn, the grid area (excluding pores) was higher, compared to model one, showing a statistically significant increase with both printing pressure and cross-linking treatment (Fig. 6b). While evaluating, a syneresis effect was observed [40], yet not being calculated, as the released water is not an integral part of the grid structure. It can be assumed that while printed as a 7-layer formation, approximately one to two layers failed to retain their shape along the Z-axis, spreading instead across the XY-axes. The 5% (LMP-XG-CNC) ink samples retained the grid shape more effectively, with a grid area closer to the model, likely due to the higher solid matter content.
Regarding the perimeter coefficient as a descriptor of the homogeneity of grid edge profiles, the values ranged from 0.86 to 0.99, resembling the model shape (Fig. 6c). Respective values for treated samples were lower compared to natural one, though not statistically significant. This is because swelling may deform a grid [40], potentially in a manner that is possibly predefined by a printing protocol. As shown in Supplementary Fig. F8, the printing protocol is prone to overlapping structures, which can form local points of over-extrusion, thereby altering pore and grid dimensions. The smoother edge surface observed in the 3% (LMP-XG-CNC) samples is attributed to the dominance of surface tension over yield stress in high-water formulations, which promotes a uniform liquid-air interface [41]. Conversely, the increased edge roughness in the 5% (LMP-XG-CNC) samples likely stems from the high solid matter content and cellulose-induced fiber drag at the nozzle wall, which prevents the ink from re-leveling post-extrusion [41].
Grid extent, a cumulative parameter describing grid width and length, was close to the initial model value (Fig. 6d), with statistically significantly higher values in the treated samples compared to the natural ones.

As an integral part of a grid, pore geometry is crucial for considering both printing strategies and the material response to the applied loads [42]. Pore area retention (Fig. 6e) can be defined as satisfactory, being in a range of 50-80% of its initial area [43]. In all cases, the values for the treated samples were lower compared to those for the natural materials, suggesting water swelling while cross-linking. Water swelling not only decreases pore perimeter (Fig. 6g) and

pore area (Fig. 6h), but also distorts the pore's shape, as evidenced by the pore factor evaluation (Fig. 6f). Being a descriptor of pore shape deviation, the data values were in around the model value, with no major dependencies between the natural and treated samples being observed (Fig. 6b). It is worth mentioning that a grid printed was initially a model of a rectangle with a grid infill, so that on 2D model scheme, pores are both observed as a large squares (*infills*), and a narrow strips (*imprints*). For the 3% (LMP-XG-CNC) samples, these narrow strips were discontinued by a slipping lines while printing, leaving an *infill* pores only. In turn, outliers were defined by the presence of interconnected pores, assuming biased structural integrity of the final prints. It allows to consider that fine-tuning of a pre-print/post-print delay is crucial here. In contrast, the pore factor of the 5% (LMP-XG-CNC) samples was almost that of the initial model, yet with broader data distribution. While for the natural samples, the data distribution was defined by the presence of *imprint* pores*,* for the treated sample, it was a matter of *infill* pore distortion and layer separation. For the treated samples, *imprints* were discontinued, which is another observation reported. It may result from syneresis-driven shrinkage, capillary effect, and filament fusion. The mechanism here may include syneresis-driven grid wall pulling inwards, together with local viscosity drop while aqueous cross-linkers are added [40]. It makes filament to slip together, distorting the delicate geometry of *imprint* pores.

3.5. Morphological characterization of 3D biomaterial structures

Polysaccharide-based cross-linked structures typically exhibit enhanced preservation of their 3D architecture, maintaining predefined macropore size and geometry, along with thinner, non-fused filaments [44]. Accordingly, in the present study, morphological evaluations were performed on cross-linked samples printed at the maximum printing pressure (Fig. 7), which ensured stable extrusion while maintaining dimensional accuracy. Following freeze-drying, the 3D-printed scaffolds retained their overall geometry and structural integrity. A similar porous microstructure has also been reported for 3D-printed polysaccharide systems by Salazar Salas et al. [45].

All formulations exhibited comparable porous architectures, characterized by randomly distributed micrometer-scale pores, as shown on representative images in Fig. 7. Apparent porosity of the 5% formulation was greater than for the 3% formulation. The average pore length was 99 ± 21 μm for the 5% formulations (Fig. 7 a), while 38 ± 13 μm for the 3% formulations (Fig. 7 b). For comparison, SEM images for two-component formulations were analysed revealing average pore size equal to 50 ± 21 μm for XG-CNC (Fig. 7 c), 72 ± 38 μm for LMP-CNC (Fig. 7 d), and 82 ± 37 μm for LMP-XG (Fig. 7 e). The cross-sectional area of scaffolds printed from the 3% ink formulation was larger than that of the 5% formulation, which can be attributed to differences in viscosity and the amount of material extruded per unit time. Due to its higher viscosity, the 5% ink resulted in lower material deposition during printing compared to the 3% formulation (Fig. 7 a, b).

A visible difference of the microstructure between two-component and three-component formulations is layered structure for the former one. Variations in layer structure and scaffold framework among different polysaccharide compositions (Fig. 7 c-e) may be attributed to differences in water-binding capacity and freezing kinetics during the freeze-drying process.

3.6. Mechanical properties of 3D-printed biomaterial structures

Macroscale mechanical properties of 3D-printed biomaterial structures, in a function of printing pressure, formulations and treatment, are shown on Fig. 8. As for the Young's modulus (Fig. 8a), the values for natural samples were somewhere in 1-11 kPa span, being in line with data reported previously [36,46,47]. Data values for the other parameters has been barely reported previously, yet showing the similar trends – increasing mechanical properties with a printing pressure (amount of material extruded), and cross-linking treatment (Fig. 8 b-d). The mechanical properties of the treated samples deviate significantly compared to the natural samples, as determined by $CaCl_2$ diffusivity and the subsequent formation of an ionic cross-linking network. The penetration of calcium ions into the polymer matrix (e.g., alginate or similar biopolymers) facilitates the 'egg-box' model of junction zones, which drastically increases the network's elastic recovery and ultimate strength. This relationship is often governed by Fick's laws of diffusion, where the concentration gradient and immersion time dictate the depth and density of the reinforced layer.

Although not a part of this current study, but usually evaluation of the mechanical properties of biomaterials is a common pathway to characterize their mouthfeel for further utilization in food production as an edible scaffolds [48]. Moreover, the obtained values in this study were on average lower to those of gummy and chewy food [49], being similar to the one reported for creamy fruits [50]. Mechanical properties of a ternary cellulose-hemicellulose-pectin formations are a complex interplay of concurrent intermolecular interactions, especially in the presence of water [51]. In such fiber networks, water acts as a plasticizer, altering interfiber interactions, overall limiting the mechanical performance of the biomaterials [52].

CONCLUSIONS

This study demonstrates that LMP–XG–CNC biomaterial inks can be rationally optimized to achieve suitable chemical, rheological, structural, and mechanical performance for 3D printing. FTIR analysis confirmed composition-dependent polysaccharide interactions, with stronger hydrogen bonding at higher solid contents and in XG-rich systems, while increased CNC loading enhanced optical whiteness through improved light scattering. Rheological optimization via a central composite design yielded statistically robust quadratic models, identifying LMP as the dominant contributor to viscosity and yield stress and producing inks with the shear-thinning and thixotropic behavior required for reliable extrusion. Shape fidelity

assessments showed a trade-off between smoothness and dimensional stability: the 3% inks formed smoother but poorly retained structures due to spreading, whereas the 5% inks exhibited rougher edges but superior line, grid, and pore retention. Mechanical testing indicated low-modulus, soft-solid behavior (1–11 kPa), which was significantly enhanced by $CaCl_2$ cross-linking through ionic "egg-box" network formation, resulting in properties comparable to creamy foods and governed by water-mediated interactions within the cellulose-based fiber network. All formulations produced porous scaffolds with randomly distributed micrometer-scale pores. The 3% inks yielded larger scaffold cross-sections due to lower viscosity and higher material deposition, while differences in internal architecture were attributed to composition-dependent water binding and freeze-drying kinetics.

ASSOCIATED CONTENT

Supporting Information.

Annex is the supplementary data related to this article.

CRediT authorship contribution statement

Smarak Bandyopadhyay: Conceptualization, Methodology, Formal analysis, Data Curation, Writing - original draft preparation, Writing - reviewing and editing, Visualization. Vadym Chibrikov: Methodology, Software, Formal analysis, Data Curation, Writing - original draft preparation, Writing - reviewing and editing, Visualization. Katarzyna Grygorczuk-Płaneta: Formal analysis, Data Curation, Writing - Original Draft. Karolina Fila: Formal analysis, Data Curation, Writing - editing. Abitha Puzhakkara Veettil: Formal analysis, Data Curation, Writing - editing. Justyna Cybulska: Methodology, Writing - Original Draft, Writing - reviewing and editing. Katarzyna Szewczuk-Karpisz: Writing - reviewing and editing. Artur Zdunek: Conceptualization, Writing - reviewing and editing, Funding acquisition. All authors have read and agreed to the published version of the manuscript.

Declaration of competing interest

The authors declare the following financial interests/personal relationships which may be considered as potential competing interests: Artur Zdunek reports financial support was provided by National Science Centre Poland. If there are other authors, they declare that they have no known competing financial interests or personal relationships that could have appeared to influence the work reported in this paper.

Data availability

Data will be made available on request.

Funding Statement

This work was supported by the *National Science Centre, Poland* as a part of *OPUS25* program (grant nr – 2023/49/B/NZ9/02979). Vadym Chibrikov is a scholarship holder benefiting from the financial support of the scholarship of the Minister of Science and Higher Education of Poland for young scientists. Grant number - SMN/21/1431/2025. Vadym Chibrikov is a scholarship holder benefiting from the financial support of the Foundation for Polish Science (FNP). Grant number - START 11.2026.

REFERENCES

1. Ee, L. Y. & Yau Li, S. F. Recent advances in 3D printing of nanocellulose: structure, preparation, and application prospects. *Nanoscale Advances* **3**, 1167–1208 (2021).
2. Yang, J. *et al.* Cellulose, hemicellulose, lignin, and their derivatives as multi-components of bio-based feedstocks for 3D printing. *Carbohydrate Polymers* **250**, (2020).
3. Bugday, Y., Alicke, A., Anderson, P. & Sman, R. van der. Understanding the large deformation response of paste-like 3D food printing inks. *Applied Rheology* **35**, (2025).
4. Agarwal, T., Costantini, M. & Maiti, T. K. Extrusion 3D printing with Pectin-based ink formulations: Recent trends in tissue engineering and food manufacturing. *Biomedical Engineering Advances* **2**, 100018 (2021).
5. Vancauwenberghe, V. *et al.* Pectin based food-ink formulations for 3-D printing of customizable porous food simulants. *Innovative Food Science & Emerging Technologies* **42**, 138–150 (2017).
6. Vancauwenberghe, V. *et al.* 3D printing of plant tissue for innovative food manufacturing: Encapsulation of alive plant cells into pectin based bio-ink. *Journal of Food Engineering* **263**, 454–464 (2019).
7. Vancauwenberghe, V., Verboven, P., Lammertyn, J. & Nicolaï, B. Development of a coaxial extrusion deposition for 3D printing of customizable pectin-based food simulant. *Journal of Food Engineering* **225**, 42–52 (2018).
8. Bahçegül, E. G., Bahçegül, E. & Özkan, N. 3D Printing of Hemicellulosic Biopolymers Extracted from Lignocellulosic Agricultural Wastes. *ACS Applied Polymer Materials* **2**, 2622–2632 (2020).
9. Gokce Bahcegul, E., Bahcegul, E. & Ozkan, N. 3D printing of crude lignocellulosic biomass extracts containing hemicellulose and lignin. *Industrial Crops and Products* **186**, 115234 (2022).
10. da Silva Bruni, A. R. *et al.* Characterization and application of active films based on commercial polysaccharides incorporating ZnONPs. *International Journal of Biological Macromolecules* **224**, 1322–1336 (2023).
11. Pombal, M., Marcet, I., Rendueles, M. & Diaz, M. Emulsifiers: Their Influence on the Rheological and Texture Properties in an Industrial Chocolate. *Molecules* **29**, (2024).
12. Talantikite, M. *et al.* Bioinspired Thermoresponsive Xyloglucan–Cellulose Nanocrystal Hydrogels. *Biomacromolecules* **22**, 743–753 (2021).

13. Cardoso, S. M., Coimbra, M. A. & Lopes da Silva, J. A. Temperature dependence of the formation and melting of pectin–Ca2+ networks: a rheological study. *Food Hydrocolloids* **17**, 801–807 (2003).
14. Merli, M. *et al.* Pectin-based bioinks for 3D models of neural tissue produced by a pH-controlled kinetics. *Front. Bioeng. Biotechnol.* **10**, 1032542 (2022).
15. Chibrikov, V. Printability, shape retention, and mechanical properties of 3D biomaterial printed structures. (2025).
16. Njoku, C. N., Otisi, S. K., Njoku, C. N. & Otisi, S. K. Application of Central Composite Design with Design Expert v13 in Process Optimization. in *Response Surface Methodology - Research Advances and Applications* (IntechOpen, 2023). doi:10.5772/intechopen.109704.
17. Abu Amr, S. S., Aziz, H. A. & Bashir, M. J. K. Application of response surface methodology (RSM) for optimization of semi-aerobic landfill leachate treatment using ozone. *Appl Water Sci* **4**, 231–239 (2014).
18. Bhattacharya, S. Central Composite Design for Response Surface Methodology and Its Application in Pharmacy. in *Response Surface Methodology in Engineering Science* (IntechOpen, 2021). doi:10.5772/intechopen.95835.
19. Barrulas, R. V. & Corvo, M. C. Rheology in Product Development: An Insight into 3D Printing of Hydrogels and Aerogels. *Gels* **9**, 986 (2023).
20. Frka-Petesic, B. *et al.* Structural Color from Cellulose Nanocrystals or Chitin Nanocrystals: Self-Assembly, Optics, and Applications. *Chem. Rev.* **123**, 12595–12756 (2023).
21. Wang, L. *et al.* Spontaneously assembled cellulose nanocrystal structural color films with tunable properties. *Sci Rep* **15**, 28840 (2025).
22. Estrada-Girón, Y., Cabrera-Díaz, E., Esparza-Merino, R. M., Martín-del-Campo, A. & Valencia-Botín, A. J. Innovative edible films and coatings based on red color pectin obtained from the byproducts of Hibiscus sabdariffa L. for strawberry preservation. *Food Measure* **14**, 3371–3380 (2020).
23. Rachtanapun, P., Suriyatemc, R. & Chaimaneed, P. Study on properties of xyloglucan / carboxymethyl cellulose blend film. in (2015).
24. Kaczmarska, A., Pieczywek, P. M., Cybulska, J., Cieśla, J. & Zdunek, A. Structural and rheological properties of diluted alkali soluble pectin from apple and carrot. *Food Chemistry* **446**, 138869 (2024).
25. Hong, T., Yin, J.-Y., Nie, S.-P. & Xie, M.-Y. Applications of infrared spectroscopy in polysaccharide structural analysis: Progress, challenge and perspective. *Food Chemistry: X* **12**, 100168 (2021).
26. Fiedot, M. *et al.* Citrus or apple inks for the 3D printing - the influence of the low methylated pectin structure and the standardized sugar type on their printability. Preprint at https://doi.org/10.26434/chemrxiv-2025-83gbg (2025).
27. Pękala, P., Szymańska-Chargot, M. & Zdunek, A. Interactions between non-cellulosic plant cell wall polysaccharides and cellulose emerging from adsorption studies. *Cellulose* **30**, 9221–9239 (2023).

28. Liu, X., Renard, C. M. G. C., Bureau, S. & Le Bourvellec, C. Revisiting the contribution of ATR-FTIR spectroscopy to characterize plant cell wall polysaccharides. *Carbohydrate Polymers* **262**, 117935 (2021).
29. Muharam, S., Yuningsih, L. M. & Sumitra, M. R. Characterization of superabsorbent hydrogel based on epichlorohydrin crosslink and carboxymethyl functionalization of cassava starch. *AIP Conf. Proc.* **1862**, 030083 (2017).
30. Figueiredo, L. R. F., Nepomuceno, N. C., Melo, J. D. D. & Medeiros, E. S. Glycerol-based polymer adhesives reinforced with cellulose nanocrystals. *International Journal of Adhesion and Adhesives* **110**, 102935 (2021).
31. Zhao, X., Qiao, L. & Wu, A.-M. Effective extraction of Arabidopsis adherent seed mucilage by ultrasonic treatment. *Sci Rep* **7**, 40672 (2017).
32. Gieroba, B., Kalisz, G., Krysa, M., Khalavka, M. & Przekora, A. Application of Vibrational Spectroscopic Techniques in the Study of the Natural Polysaccharides and Their Cross-Linking Process. *Int J Mol Sci* **24**, 2630 (2023).
33. Fellah, A., Anjukandi, P., Waterland, M. R. & Williams, M. A. K. Determining the degree of methylesterification of pectin by ATR/FT-IR: Methodology optimisation and comparison with theoretical calculations. *Carbohydrate Polymers* **78**, 847–853 (2009).
34. Popescu, C.-M. *et al.* Vibrational spectroscopy and X-ray diffraction methods to establish the differences between hardwood and softwood. *Carbohydrate Polymers* **77**, 851–857 (2009).
35. Fiedot, M. *et al.* The smart apple-based foil: The role of pectin-glycerol-lipid interactions on thermoresponsive mechanism. *Food Hydrocolloids* **154**, 110067 (2024).
36. Pitton, M. *et al.* 3D Bioprinting of Pectin-Cellulose Nanofibers Multicomponent Bioinks. *Front. Bioeng. Biotechnol.* **9**, (2021).
37. Kyle, S., Jessop, Z. M., Al-Sabah, A. & Whitaker, I. S. 'Printability' of Candidate Biomaterials for Extrusion Based 3D Printing: State-of-the-Art. *Advanced Healthcare Materials* **6**, 1700264 (2017).
38. Schwab, A. *et al.* Printability and Shape Fidelity of Bioinks in 3D Bioprinting. *Chem. Rev.* **120**, 11028–11055 (2020).
39. Farzadi, A. *et al.* Effect of layer printing delay on mechanical properties and dimensional accuracy of 3D printed porous prototypes in bone tissue engineering. *Ceramics International* **41**, 8320–8330 (2015).
40. Vancauwenberghe, V. *et al.* Pectin based food-ink formulations for 3-D printing of customizable porous food simulants. *Innovative Food Science & Emerging Technologies* **42**, 138–150 (2017).
41. Siqueira, G. *et al.* Cellulose Nanocrystal Inks for 3D Printing of Textured Cellular Architectures. *Adv Funct Materials* **27**, 1604619 (2017).
42. Perez, R. A. & Kim, H.-W. Core–shell designed scaffolds for drug delivery and tissue engineering. *Acta Biomaterialia* **21**, 2–19 (2015).
43. He, Y. *et al.* Research on the printability of hydrogels in 3D bioprinting. *Sci Rep* **6**, 29977 (2016).

44. Milojević, M. *et al.* Hybrid 3D Printing of Advanced Hydrogel-Based Wound Dressings with Tailorable Properties. *Pharmaceutics* **13**, (2021).
45. Salazar Salas, B. M. *et al.* 3D-Printed Polysaccharide Scaffolds with NIR-Triggered Activity for Diabetic Wound Healing. *ACS Omega* **10**, 43012–43023 (2025).
46. Markov, P. A. *et al.* Mechanical properties, structure, bioadhesion, and biocompatibility of pectin hydrogels. *Journal of Biomedical Materials Research Part A* **105**, 2572–2581 (2017).
47. Xu, W. *et al.* Surface Engineered Biomimetic Inks Based on UV Cross-Linkable Wood Biopolymers for 3D Printing. *ACS Appl. Mater. Interfaces* **11**, 12389–12400 (2019).
48. Souto, A., Zhang, J., Aragón, A. M., Velikov, K. P. & Coulais, C. Edible mechanical metamaterials with designed fracture for mouthfeel control. *Soft Matter* **18**, 2910–2919 (2022).
49. Williams, S. H., Wright, B. W., Truong, V. den, Daubert, C. R. & Vinyard, C. J. Mechanical properties of foods used in experimental studies of primate masticatory function. *American Journal of Primatology* **67**, 329–346 (2005).
50. Jahanbakhshi, A., Yeganeh, R. & Shahgoli, G. Determination of Mechanical Properties of Banana Fruit under Quasi-Static Loading in Pressure, Bending, and Shearing Tests. *International Journal of Fruit Science* **20**, 314–322 (2020).
51. Broxterman, S. E. The architecture of the primary plant cell wall: the role of pectin reconsidered. (2018).
52. Chibrikov, V., Pieczywek, P. M., Cybulska, J. & Zdunek, A. Evaluation of elasto-plastic properties of bacterial cellulose-hemicellulose composite films. *Industrial Crops and Products* **205**, 117578 (2023).

Figure Captions

Fig. 1 | Normal probability plots of the standardized residual for (a) viscosity at low shear rate (μ *at* $1s^{-1}$ γ), (b) high shear rate (μ *at* $100s^{-1}$ γ) and (c) yield stress (σ_γ), generated by Design-Expert

Fig. 2 | Desirability surface contour plot for the multi-objective optimization of ink formulations based on their rheological properties. Abbreviation *LM* stands for *low methylated pectin*, *XG* for *xyloglucan*, *C* for *cellulose nanocrystals, df* for *degree of freedom*, μ for *viscosity,* σy for *yield stress.*

Fig. 3 | Shear thinning behavior of two inks selected for strength evaluations of printed structure. Abbreviation *LMP* stands for *low methylated pectin*; *XG* for *xyloglucan; CNC* for *cellulose nanocrystals.*

Fig. 4 | Fourier-transformed infrared spectra of (a) spectra from 3d structures of composites containing different pairs of polysaccharides and (b) differential spectra between ink formulation and 3d structure. Abbreviation *LMP* stands for *low methylated pectin*; *XG* for *xyloglucan; CNC* for *cellulose nanocrystals.*

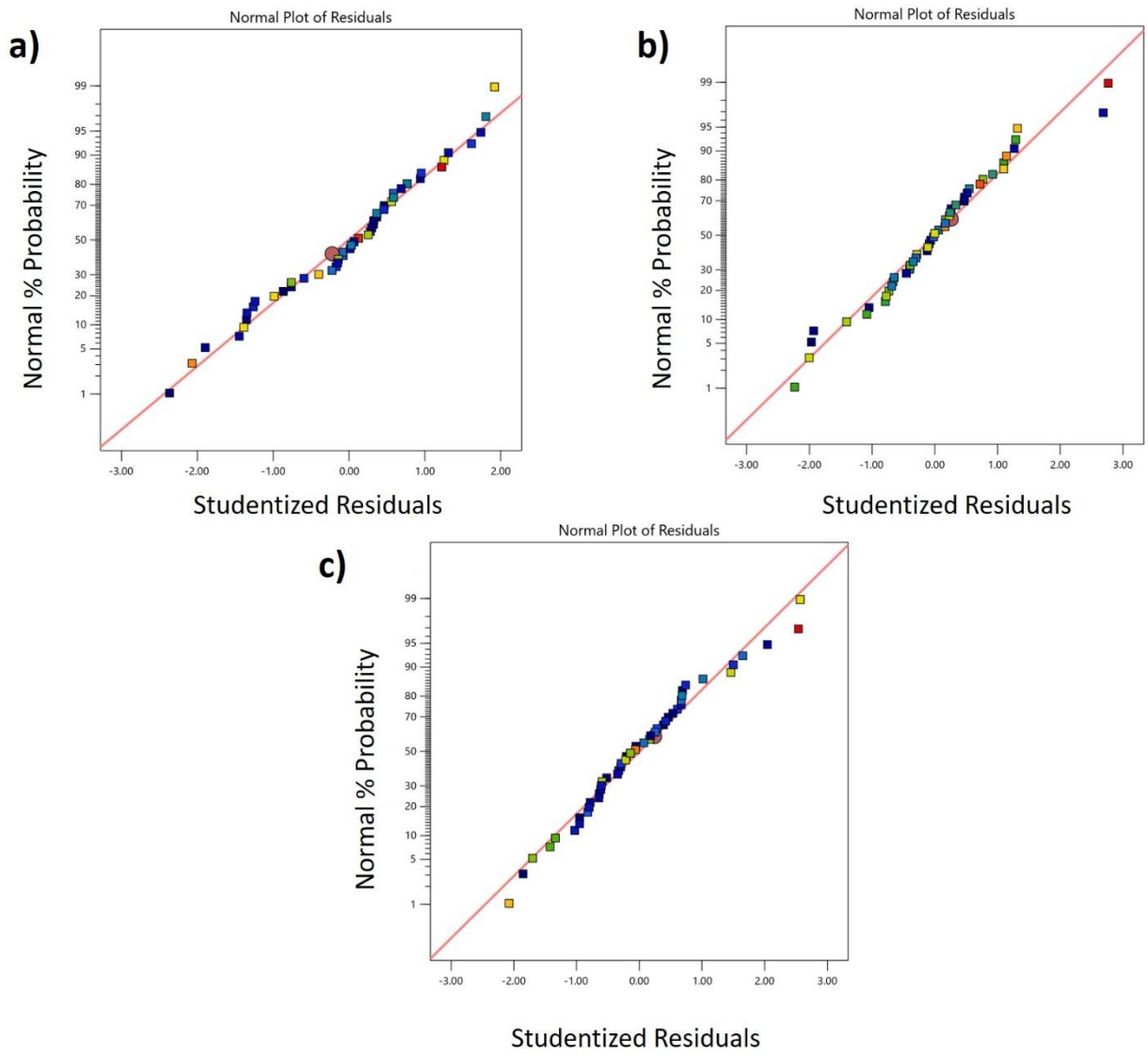
Fig. 5 | Shape retention properties of 3D biomaterial printed lines: a) uniformity factor; b) line width; c) line length. For subfigures a-b), data points and bars represent mean values and standard deviation, respectively; for subfigure c), data are presented as a box plot with individual data points overlaid. For a two-way (ink composition and printing pressure) analysis of variance (ANOVA), treatments labelled with the same letters show a lack of statistically significant differences between the samples ($p > 0.05$). For subsequent subfigures, dashed lines represent the model value (reference), while the photos in subsequent columns represent exemplary printed lines. Abbreviation *CNC* stands for *cellulose nanocrystals*; *LMP* for *low-methylated pectin*; *MAD* for *median absolute deviation*; *n* for *number of replications*; S*D* for *standard deviation*; *XG* for *xyloglucan.*

Fig. 6 | Shape retention properties of 3D biomaterial printed grids: a) total grid area; b) grid area; c) perimeter coefficient; d) grid extent; e) pore area retention; f) pore factor; g) pore perimeter; h) pore area. For subfigures a), b), c), e), data points and bars represent mean values and standard deviation, respectively; for subfigures d), f), g), h), data are presented as a box plot with individual data points overlaid. For a three-way (ink composition, printing pressure, and cross-linking treatment) analysis of variance (ANOVA), treatments with the same letters show a lack of statistically significant differences between the samples ($p > 0.05$). For subsequent subfigures, dashed lines represent the model value (reference), while the photos/pictograms in subsequent

columns represent exemplary printed grids/models, respectively. Abbreviation *CNC* stands for *cellulose nanocrystals*; *LMP* for *low-methylated pectin*; *MAD* for *median absolute deviation; n* for *number of replications SD* for *standard deviation*; *XG* for *xyloglucan*.

Fig. 7 | Cross-sectional SEM micrographs of lyophilized 3D printed grids printed at maximum printing pressures. *LMP. Low Methylated Pectin, CNC. Cellulose Nano Crystals, XG. Xyloglucan.*

Fig. 8 | Mechanical properties of 3D biomaterial printed cylinders: a) Young's modulus; b) maximum stress; c) toughness; d) total work. For all subfigures, data are presented as a box plot with individual data points overlaid. For a three-way (ink composition, printing pressure, and cross-linking treatment) analysis of variance (ANOVA), treatments with the same letters show a lack of statistically significant differences between the samples ($p > 0.05$). Abbreviation *CNC* stands for *cellulose nanocrystals*; *LMP* for *low-methylated pectin*; *MAD* for *median absolute deviation*; *n* for *number of replications*; *XG* for *xyloglucan*.

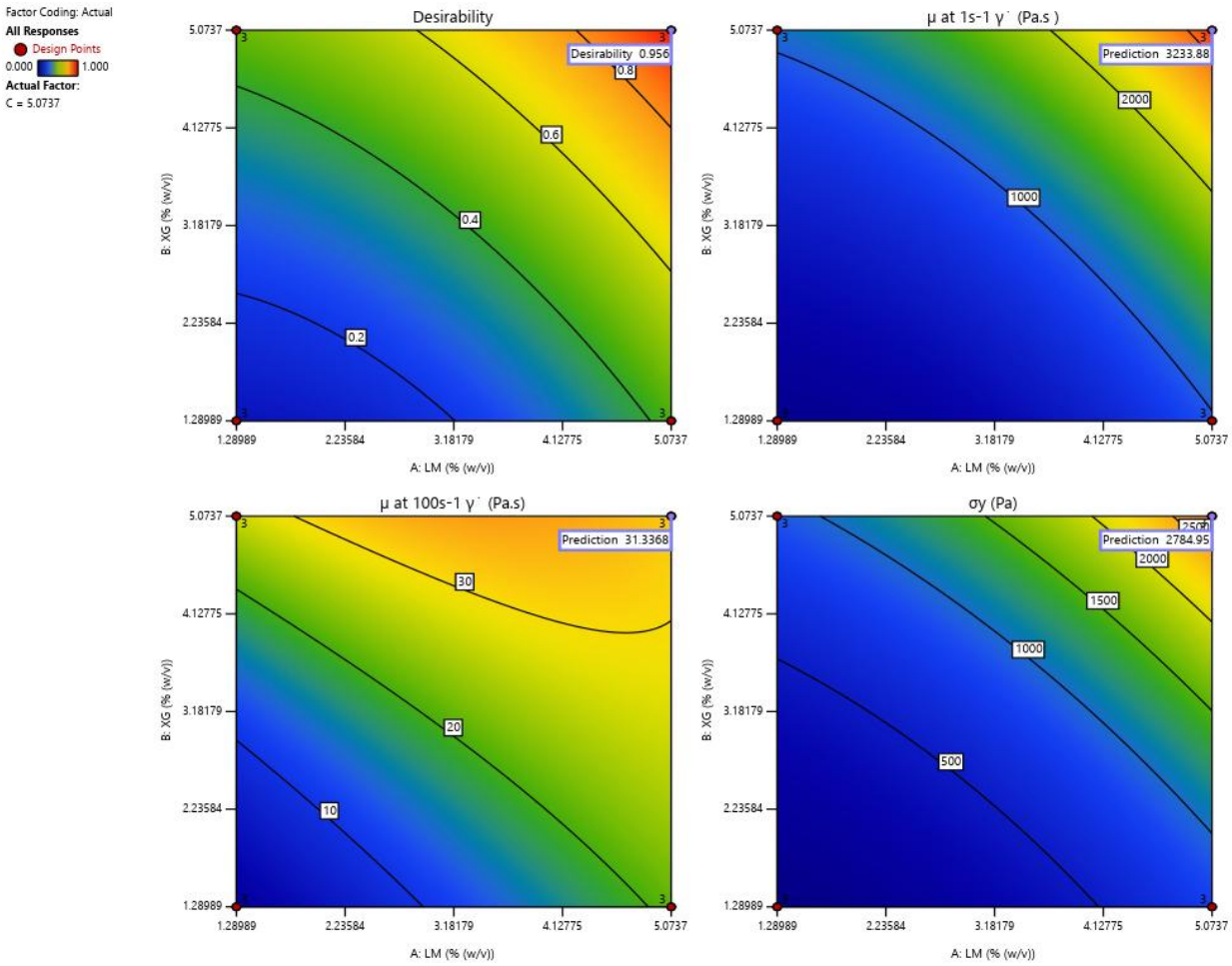


775

776 **Figure 1** Normal probability plots of the standardized residual for (a) viscosity at low shear rate

777 (μ *at* $1s^{-1}$ γ), (b) high shear rate (μ *at* $100s^{-1}$ γ) and (c) yield stress (σ_y), generated by Design-Expert

778



779

780 **Figure 2** Desirability surface contour plot for the multi-objective optimization of ink formulations
781 based on their rheological properties. Abbreviation *LM* stands for *low methylated pectin*, *XG* for
782 *xyloglucan*, *C* for *cellulose nanocrystals, df* for *degree of freedom*, *μ* for *viscosity, σy* for *yield*
783 *stress.*

784

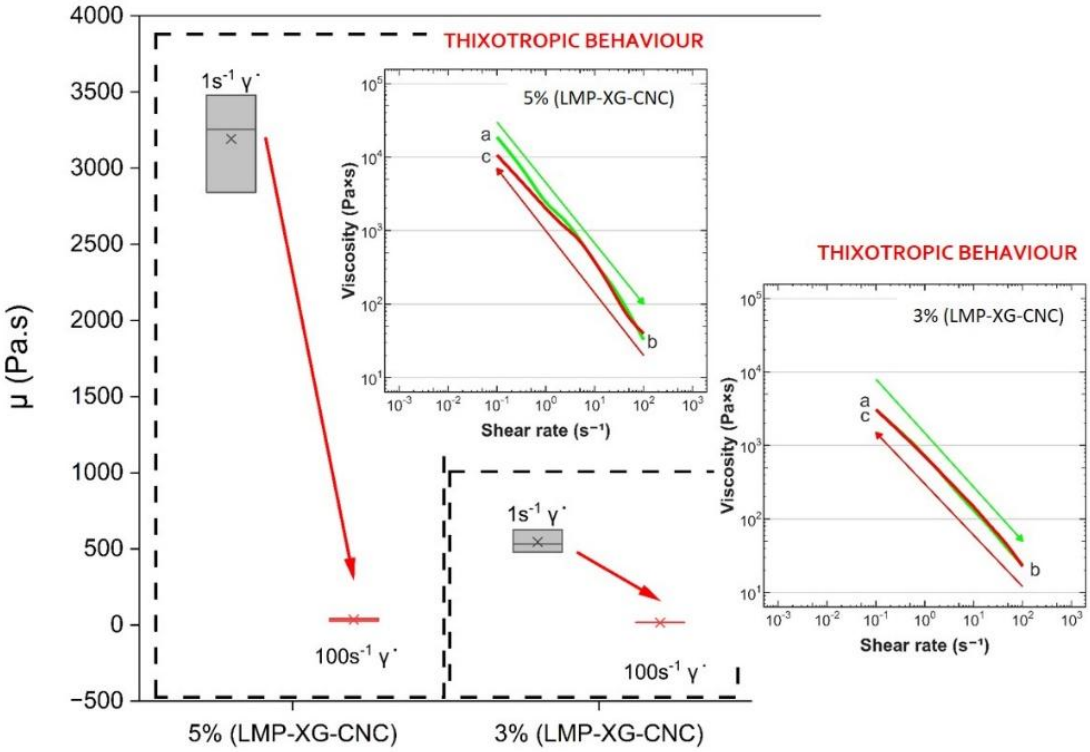
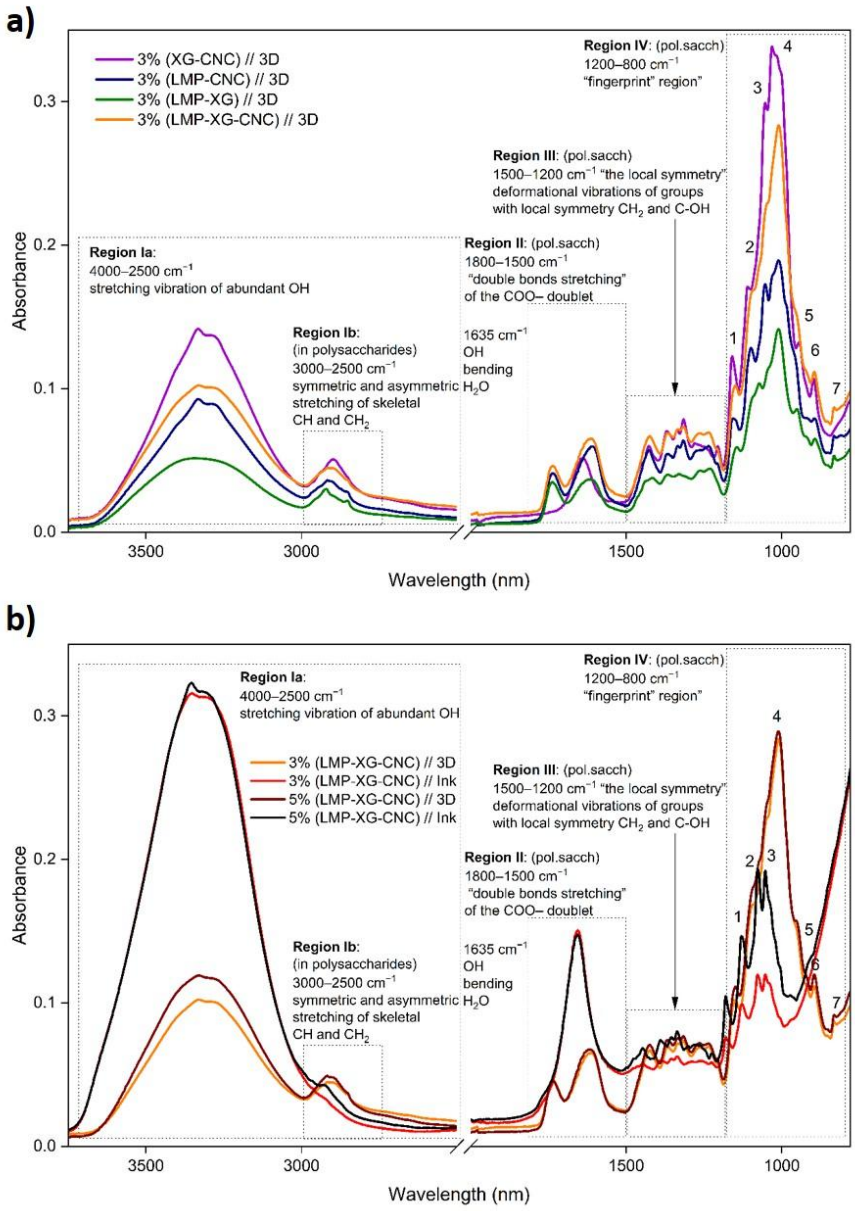


Figure 3 Shear thinning behavior of two inks selected for strength evaluations of printed structure. Abbreviation *LMP* stands for *low methylated pectin*; *XG* for *xyloglucan; CNC* for *cellulose nanocrystals.*



790

791 **Figure 4** Fourier-transformed infrared spectra of (a) spectra from 3d structures of composites
792 containing different pairs of polysaccharides and (b) differential spectra between ink formulation
793 and 3d structure. Abbreviation *LMP* stands for *low methylated pectin*; *XG* for *xyloglucan; CNC*
794 for *cellulose nanocrystals.*

795

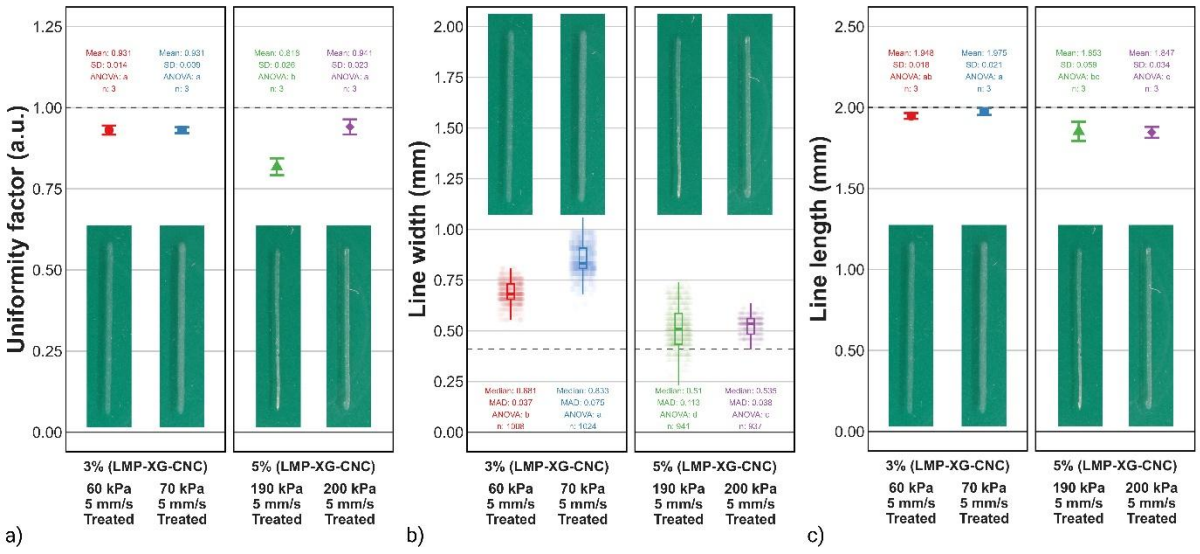
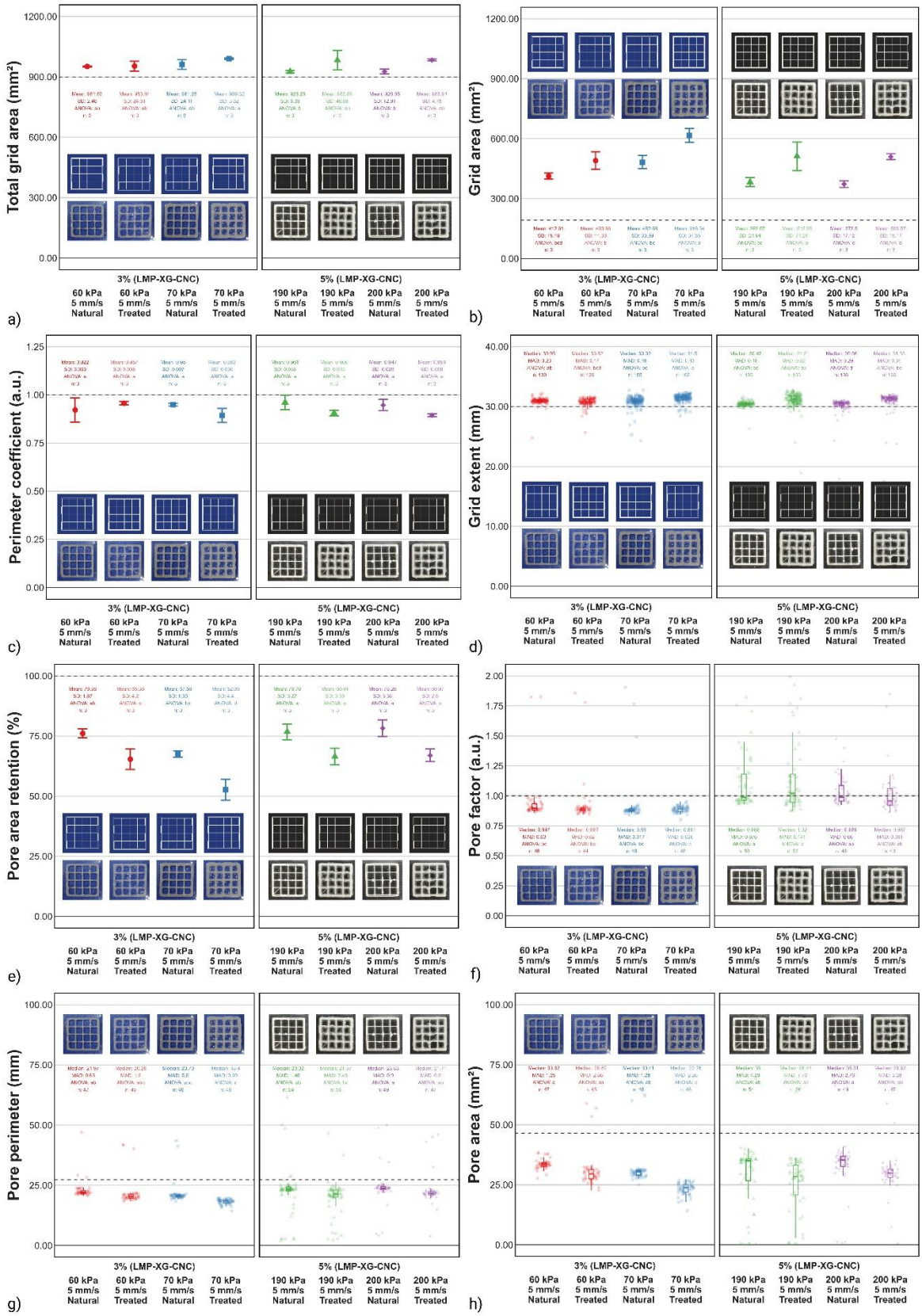


Figure 5 Shape retention properties of 3D biomaterial printed lines: a) uniformity factor; b) line width; c) line length. For subfigures a-b), data points and bars represent mean values and standard deviation, respectively; for subfigure c), data are presented as a box plot with individual data points overlaid. For a two-way (ink composition and printing pressure) analysis of variance (ANOVA), treatments labelled with the same letters show a lack of statistically significant differences between the samples ($p > 0.05$). For subsequent subfigures, dashed lines represent the model value (reference), while the photos in subsequent columns represent exemplary printed lines. Abbreviation *CNC* stands for *cellulose nanocrystals*; *LMP* for *low-methylated pectin*; *MAD* for *median absolute deviation*; *n* for *number of replications*; S*D* for *standard deviation*; *XG* for *xyloglucan.*


Total grid area (mm²)
Grid area (mm²)
Perimeter coefficient (a.u.)
Grid extent (mm)
Pore area retention (%)
Pore factor (a.u.)
Pore perimeter (mm)
Pore area (mm²)
3% (LMP-XG-CNC)
5% (LMP-XG-CNC)
60 kPa 5 mm/s Natural
60 kPa 5 mm/s Treated
70 kPa 5 mm/s Natural
70 kPa 5 mm/s Treated
190 kPa 5 mm/s Natural
190 kPa 5 mm/s Treated
200 kPa 5 mm/s Natural
200 kPa 5 mm/s Treated
a)
b)
c)
d)
e)
f)
g)
h)

807

Figure 6 Shape retention properties of 3D biomaterial printed grids: a) total grid area; b) grid area; c) perimeter coefficient; d) grid extent; e) pore area retention; f) pore factor; g) pore perimeter; h) pore area. For subfigures a), b), c), e), data points and bars represent mean values and standard deviation, respectively; for subfigures d), f), g), h), data are presented as a box plot with individual data points overlaid. For a three-way (ink composition, printing pressure, and cross-linking treatment) analysis of variance (ANOVA), treatments with the same letters show a lack of statistically significant differences between the samples ($p > 0.05$). For subsequent subfigures, dashed lines represent the model value (reference), while the photos/pictograms in subsequent columns represent exemplary printed grids/models, respectively. Abbreviation *CNC* stands for *cellulose nanocrystals*; *LMP* for *low-methylated pectin*; *MAD* for *median absolute deviation; n* for *number of replications SD* for *standard deviation*; *XG* for *xyloglucan*.

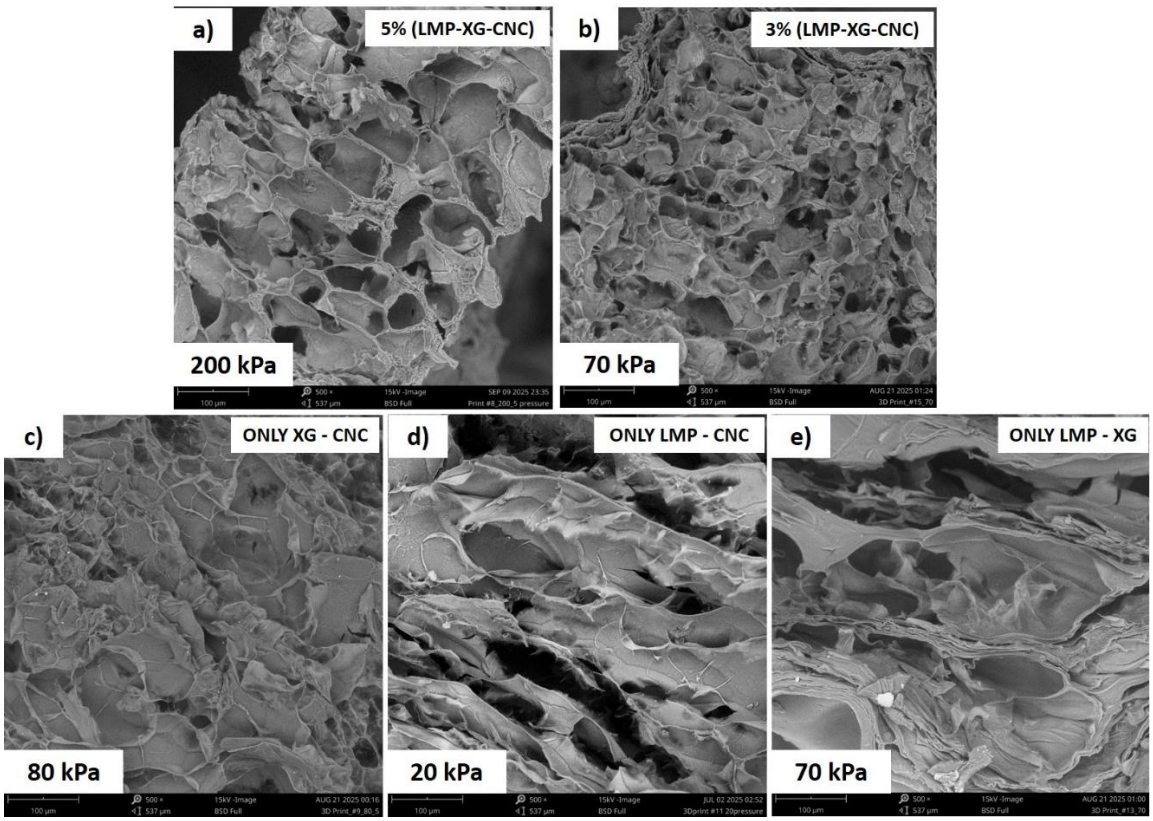


Figure 7 Cross-sectional SEM micrographs of lyophilized 3D printed grids printed at maximum printing pressures. *LMP. Low Methylated Pectin, CNC. Cellulose Nano Crystals, XG. Xyloglucan.*

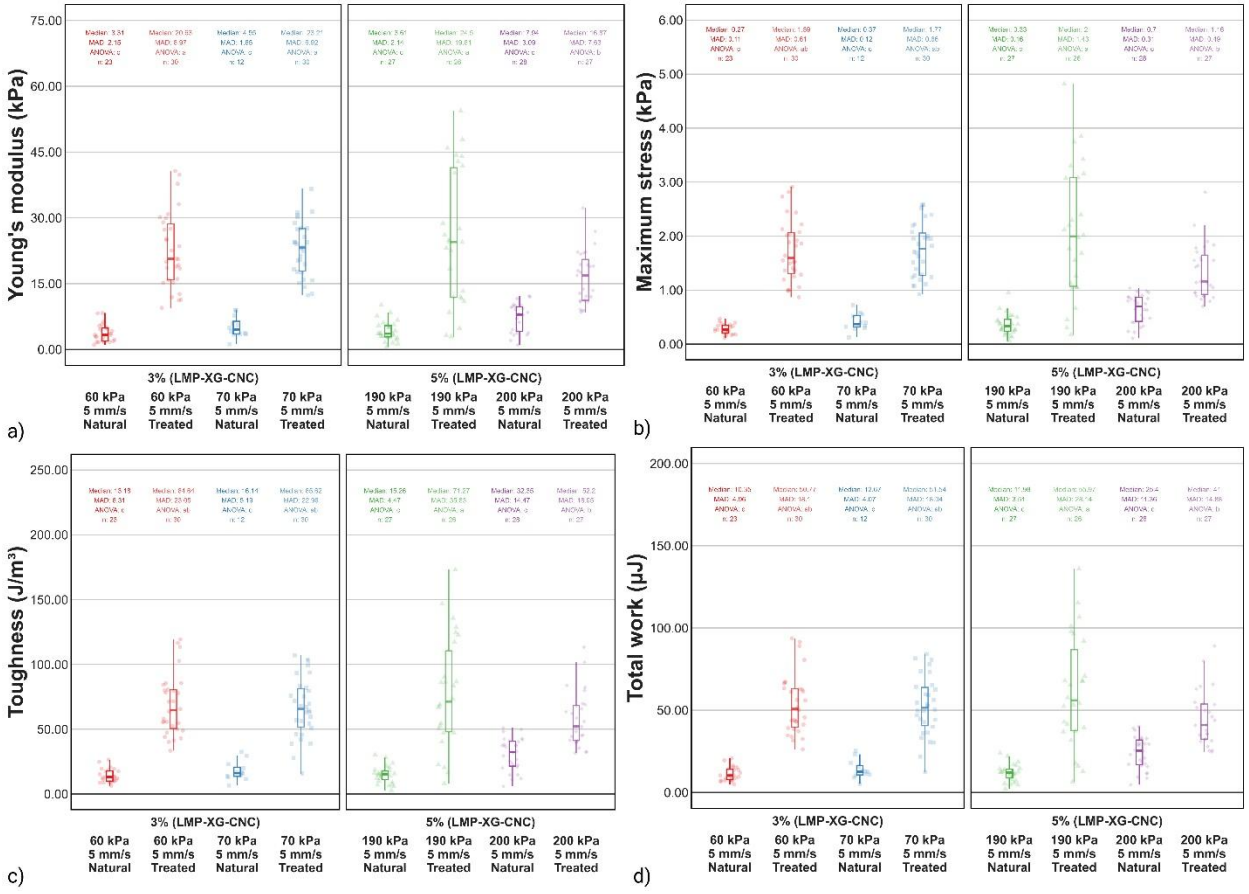


Figure 8 Mechanical properties of 3D biomaterial printed cylinders: a) Young's modulus; b) maximum stress; c) toughness; d) total work. For all subfigures, data are presented as a box plot with individual data points overlaid. For a three-way (ink composition, printing pressure, and cross-linking treatment) analysis of variance (ANOVA), treatments with the same letters show a lack of statistically significant differences between the samples ($p > 0.05$). Abbreviation *CNC* stands for *cellulose nanocrystals*; *LMP* for *low-methylated pectin*; *MAD* for *median absolute deviation*; *n* for *number of replications*; *XG* for *xyloglucan*.

Supplementary Files

This is a list of supplementary files associated with this preprint. Click to download.

- AnnexSupplementary.docx